npj | quantum materials

Article

Published in partnership with Nanjing University

https://doi.org/10.1038/s41535-024-00661-3

Competition between *d*-wave superconductivity and magnetism in uniaxially strained Sr_2RuO_4

Jonas B. Profe [1,2] ✉, Sophie Beck [2], Dante M. Kennes [1,3], Antoine Georges [2,4,5,6] & Olivier Gingras [2]

The pairing symmetry of Sr_2RuO_4 is a long-standing fundamental question in the physics of superconducting materials with strong electronic correlations. We use the functional renormalization group to investigate the behavior of superconductivity under uniaxial strain in a two-dimensional realistic model of Sr_2RuO_4 obtained with density functional theory and incorporating the effect of spin-orbit coupling. We find a dominant $d_{x^2-y^2}$ superconductor mostly hosted by the d_{xy}-orbital, with no other closely competing superconducting state. Within this framework, we reproduce the experimentally observed enhancement of the critical temperature under strain and propose a simple mechanism driven by the density of states to explain our findings. We also investigate the competition between superconductivity and spin-density wave ordering as a function of interaction strength. By comparing theory and experiment, we discuss constraints on a possible degenerate partner of the $d_{x^2-y^2}$ superconducting state.

Almost 30 years after the discovery of superconductivity in Sr_2RuO_4 (SRO)[1], the symmetry of its superconducting order parameter (SCOP) remains an open question. Initially, its similarities with ^{3}Helium made it a prime candidate for spin-triplet pairing[2], corroborated by various measurements[3–11]. Along with observations of time-reversal symmetry breaking (TRSB) supporting a two-component order parameter[12,13], the superconducting (SC) state was believed for a long time to be a chiral p-wave spin-triplet. However, conflicting evidence presented in various studies remained to be explained[14,15]. First, the presence of nodal excitations is unexpected in a chiral p-wave SC[16–19]. Second, the low critical field H_{c2} exhibited by SRO is typical for Pauli-limited spin-singlet SC[20] and the transition into the normal state upon applying a magnetic field appears to be first-order[21,22], with indications of a Fulde-Ferrell-Larkin-Ovchinnikov state for a certain parameter range, strongly pointing to a singlet SCOP[23]. Third, none of the topologically protected edge states predicted in chiral p-wave states were observed in experiments[24–27], although this could be explained by a high Chern number[28].

In recent years, the chiral p-wave picture has basically been dismissed. First, the careful replications of key nuclear magnetic resonance experiments previously interpreted as supporting spin-triplet pairing have highlighted a heating effect and instead concluded that the SCOP corresponds to spin-singlet pairs[29–31]. Second, applying uniaxial strain along the x principal crystallographic axis was found to enhance the critical temperature (T_c)[32,33] and to lower the Fermi-liquid coherence scale[34]. This enhancement was shown to be maximal where the FS undergoes a Lifshitz transition, corresponding to a van-Hove singularity (vHs) in the density of states (DOS), at a time-reversal invariant momentum point, inconsistent with odd-parity SCOPs like p-wave[35]. Nowadays, a consensus appears to be crystallizing around the spin-singlet and even-parity natures of the SCOP, yet the debate is still ongoing. While ultrasound experiments support the conclusion of a two-component order parameter[36,37] inferred by the observation of TRSB and the splitting between T_c and the TRSB transition temperature[38,39], there are no two-temperature signatures in bulk thermodynamical experiments such as specific heat and elastocalorimetry as well as scanning SQUID microscopy[40–43]. As a result of this plethora of experimental evidence, SRO can be seen both as a critical playground for testing theories with the goal of potentially unifying some of these contradicting observations and as a testbed to verify whether our interpretations of specific experiments are valid. Either way, it constitutes an ideal system to

[1]Institute for Theoretical Solid State Physics, RWTH Aachen University and JARA Fundamentals of Future Information Technology, 52062 Aachen, Germany. [2]Center for Computational Quantum Physics, Flatiron Institute, 162 Fifth Avenue, New York, NY 10010, USA. [3]Max Planck Institute for the Structure and Dynamics of Matter and Center Free-Electron Laser Science, Hamburg, Germany. [4]Collège de France, Université PSL, 11 Place Marcelin Berthelot, 75005 Paris, France. [5]Centre de Physique Théorique, Ecole Polytechnique, CNRS, Institut Polytechnique de Paris, 91128 Palaiseau Cedex, France. [6]DQMP, Université de Genève, 24 Quai Ernest Ansermet, 1211 Genève, Suisse. ✉e-mail: jonas.hauck@rwth-aachen.de

considerably advance our understanding of the mechanisms for unconventional superconductivity[44].

Many theoretical proposals have been put forward as potential SCOPs. Initially classified as a chiral p-wave[45–52], the recent experimental evidence motivated further proposals, including two-dimensional states such as $s + id_{xy}$[53–56], $d_{x^2-y^2} + ig_{xy(x^2-y^2)}$[56–61], a combination of even and odd-parity irreducible representations (irreps)[62], inter-orbital pairing[63,64], $d + d$[65], and $d_{x^2-y^2}$ (plus odd-frequency)[66–69]. Some three-dimensional states were also proposed, for example, $E_g\ d_{yz} + id_{zx}$[70,71] and helical $p_x + p_y$[72].

A general overview of possible ordering states in terms of their irreducible representations is given in refs. 63,73.

In this paper, we investigate the leading superconducting instabilities of SRO using functional renormalization group (FRG) calculations[74], applied to a realistic model of the electronic structure derived from density functional theory (DFT)[75] that includes spin-orbit coupling (SOC). Note that previous studies of SRO using FRG were performed on tight-binding models, fitted to photoemission spectroscopy measurements[46,48,59,76–78]. In order to compare to experiments, we study the effect of uniaxial strain, tracking the evolution of T_c as well as the type of ordering. We find a phase diagram with two different magnetic orders that compete with a single SCOP transforming like the B_{1g} irrep (often labeled as $d_{x^2-y^2}$-wave). This competition is found to depend sensitively on the choice of interaction parameters. We show that a proper range of parameters leads to an increase of the superconducting T_c in good agreement with experiments.

Methods

Density functional theory

We use DFT[75,79,80] and the Quantum ESPRESSO DFT package[81,82] with the PBE exchange-correlation functional[83] to calculate the electronic structure. Cell parameters and internal coordinates of the crystal structure in the *I*4/*mmm* space group are relaxed in the conventional cell until all force components are smaller than 1 mRy/a_0 (a_0: Bohr radius) and all components of the stress tensor are smaller than 0.5 kbar, yielding a relaxed in-plane (out-of-plane) lattice constant of $a_0 = 3.878$ Å ($c = 12.900$ Å). To calculate the strained structures, we fix one in-plane lattice constant of the conventional cell to the strained value, $a_{new} = (1 - s)a_0$, and relax the two orthogonal cell parameters as well as the internal coordinates as described above. After relaxation, we use the corresponding primitive unit cells containing one ruthenium atom each, i.e., three t_{2g} orbitals. We use scalar-relativistic ultrasoft pseudopotentials from the GBRV library[84], with the 4*s* and 4p (2*s*) semicore states for both strontium and ruthenium (for oxygen) atoms included in the valence. In the scalar-relativistic approximation, the spin-orbit coupling term is dropped[85]. The energy cutoffs for the wave functions and charge density are set to 60 Ry and 720 Ry, respectively. We use a $12 \times 12 \times 12$ Monkhorst-Pack *k*-point grid to sample the Brillouin-zone and a smearing of 0.01 Ry utilizing the Methfessel-Paxton scheme. To describe the low-energy physics we construct three ruthenium-centered t_{2g}-like maximally localized Wannier functions for each strained structure using Wannier90[86–88]. Spin-orbit coupling is included by first performing the DFT calculation without it and then adding a local SOC $\lambda_{SOC} = 200$ meV to account for the correlation-induced enhancement over the DFT value.

Functional renormalization group

In order to account for strong local electronic correlations in this multi-orbital system, we consider the Hubbard-Kanamori interaction Hamiltonian[89]

$$\begin{aligned}\hat{H}_{\text{int}} = &\sum_{\text{il}} U\hat{n}^{\uparrow}_{\text{il}}\hat{n}^{\downarrow}_{\text{il}} + \sum_{\text{il}_1\neq\text{il}_2}(U-2J_{\text{dd}})\hat{n}^{\uparrow}_{\text{il}_1}\hat{n}^{\downarrow}_{\text{il}_2}\\ &+ \sum_{\text{i}\sigma\text{l}_1\neq\text{l}_2}(U-3J_{\text{dd}})\hat{n}^{\sigma}_{\text{il}_1}\hat{n}^{\sigma}_{\text{il}_2}\\ &- \sum_{\text{il}_1\neq\text{l}_2} J_{\text{ss}}\hat{c}^{\uparrow,\dagger}_{\text{il}_1}\hat{c}^{\downarrow}_{\text{il}_1}\hat{c}^{\downarrow,\dagger}_{\text{il}_2}\hat{c}^{\uparrow}_{\text{il}_2} + \sum_{\text{il}_1\neq\text{l}_2} J_{\text{ss}}\hat{c}^{\uparrow,\dagger}_{\text{il}_1}\hat{c}^{\downarrow,\dagger}_{\text{il}_1}\hat{c}^{\downarrow}_{\text{il}_2}\hat{c}^{\uparrow}_{\text{il}_2}\end{aligned} \tag{1}$$

where U is the intra-orbital on-site Coulomb repulsion, while J_{dd} (J_{ss}) is the density-density (spin-flip and pair hoping) part of the Hund's coupling. In the rotationally invariant formulation where $O(3)$ symmetry is satisfied, $J_{dd} = J_{ss} = J$. Although usually equal, the distinct effect of J_{dd} and J_{ss} when they are treated independently is discussed in Supplementary Note 2. Our calculations are performed in the regime of $U/W = 0.3 - 0.5$, with W being the total bandwidth and U being the Hubbard interaction. We restrict ourselves to a situation with an on-site Hubbard-Kanamori interaction, as with this type of interaction, we reproduce the dominant spin-spin susceptibilities peak position in comparison to the interacting spin-spin susceptibility measured in neutron scattering experiments[90], see Supplementary Note 2. Any interaction resulting in an analog peak structure should give the same physical results, as we argue in Supplementary Note 5.

The strong electronic correlations emerging from the Hubbard-Kanamori interactions are incorporated to the non-interacting downfolded systems using the FRG[74,91]. FRG is technically an exact method to calculate the effective action function of a given quantum action. It does so by introducing a scale-dependent cutoff (here we use a sharp energy cutoff) in the non-interacting propagator of the system. By taking derivatives with respect to this cutoff, one generates an infinite hierarchy of flow equations. In practice, this hierarchy must be truncated to become numerically tractable, making the method perturbatively motivated.

In this work, we employ the standard level-2 truncation, neglecting all three and more particle vertices. The validity of this approximation in the weak-to-intermediate coupling regime can be motivated by a power-counting argument to prove the RG-irrelevance of higher-order terms[74]. Furthermore, we neglect the frequency dependence of the interaction, again motivated by the power-counting argument and the self-energy. This approach was applied to various systems including SRO[46,48,76–78,92–103] and can be viewed as a diagrammatically unbiased extension of the random phase approximation.

In practice, we solve the flow equations from an energy scale much larger than the bandwidth and then integrate towards lower energies until we hit a divergence in one of the three diagrammatic channels labeled the particle-particle (PP), particle-hole (PH), and crossed particle-hole ($\overline{\text{PH}}$) channels. A divergence is associated with a phase transition as the corresponding susceptibility also diverges. Information on the ordering type can be extracted from the susceptibilities as well as linearized gap equations[104].

We employ the truncated unity approximation which allows us to reduce the memory required computationally[105–107].

For the FRG simulations, we use the TU^{2}FRG code[107]. For convergence, we include all form-factors up to a distance of 8.2 Å, which amounts to a total number of 75 basis functions per orbital in the unit cell, i.e., all lattice harmonics up to the fifth (sixth) are included (depending on whether the constant is counted as harmonic or not). We checked for convergence by increasing the number of form-factors included near the phase transition between the magnetic and the superconducting phase for a few data points in the phase diagram. The simulations are performed on a 36×36 momentum-mesh in the $x - y$ plane for the vertex function. The loop integration is performed using a FFT approach and an additional refinement of 45×45 is employed to achieve higher energy resolution. The results of the integration do not differ upon changing the resolution of the loop integration.

By using an enhanced value of the SOC, the effects of local interactions on SOC are already included on the single-particle level of the calculations. We do not suffer from double counting at that level since we neglect the flow of the self-energy. As a consequence, however, our calculation does not take into account the renormalized effective mass of quasi-particles.

Results

Electronic structure

To describe the low-energy electronic structure of SRO for the different strain values, we perform ab initio DFT calculations downfolded onto the t_{2g} orbitals of the ruthenium atoms using maximally localized Wannier functions as detailed in the methods section. There is extensive literature using tight-binding Hamiltonians from ab initio electronic structure calculations

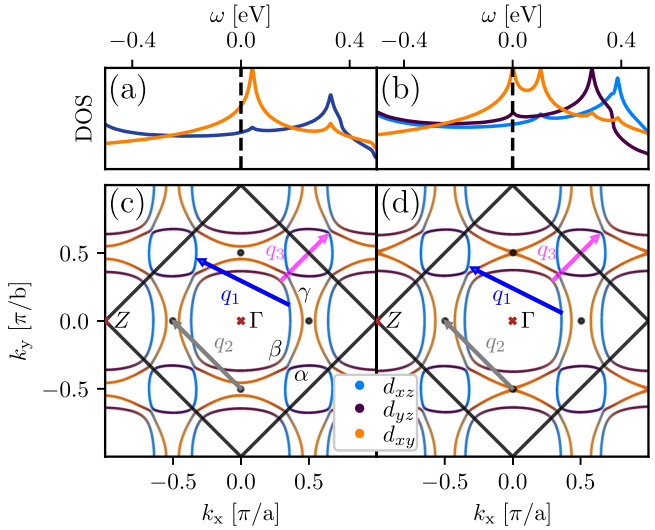

Fig. 1 | Partial density of states and Fermi surface for the three t_{2g} orbitals. Unstrained (**a**, **c**) and the optimally strained (**b**, **d**) systems. The optimal stain of 0.8% corresponds to the system being closest to the Lifshitz transition. Here, a (b) is the lattice parameter in the x (y) direction, with $a = b$ in the $\epsilon_{xx} = 0$ case. The black dots indicate the position of the vHs of the d_{xy} orbital. The three dominant spin-density wave ordering vectors q_1, q_2, and q_3 are highlighted in black, gray, and pink, respectively. The first Brillouin-zone is marked by a black square. We mark the Γ and Z points by red crosses. Furthermore, we labeled the α, β, and γ sheets on the FS for $\epsilon_{xx} = 0$. In the unstrained case, the partial DOS for the d_{xz} and d_{yz} orbitals is identical, which is emphasized by the color mixing.

based on DFT for SRO, presenting overall very consistent results at the DFT level. Beyond DFT, it was shown that replacing the local SOC parameter of 100 meV obtained within DFT with a value twice as large $\lambda_{SOC} \simeq 200$ meV yielded a considerably better agreement with the experimentally observed Fermi surface[108], in consistent with the correlation-induced enhancement predicted theoretically[109,110]. Indeed, this parameter adjustment leads to improved agreement with the FS both in the unstrained case and with the experimentally observed critical strain[108–115]. A comparison to a selection of previously published tight-binding models is shown in Supplementary Note 1. Note that the addition of SOC breaks the $SU(2)$ spin symmetry, but preserves an orbitally dependent $SU(2)$ (so-called pseudospin) symmetry[68]. We keep the SOC fixed for all strain values.

In order to account for strong electronic correlations in this multi-orbital system, we use for most parts of this paper the $O(3)$ symmetric Hubbard-Kanamori parametrization of the interaction Hamiltonian[89], which involves two key energy scales: the on-site Hubbard repulsion U and the Hund coupling J - see methods. As done routinely in FRG calculations[46,48,76–78,92–103], we neglect the flow of the self-energy in our calculations. Hence, the interaction parameters (U, J) should be considered as effective interactions with significance within our FRG framework rather than having a first-principle meaning. In this perspective, it is important to explore how the various instabilities are tuned by varying the interaction parameters. The guiding principles for constructing the model utilized follow two rules

- We start from state-of-the-art DFT with added spin-orbit coupling λ_{SOC} such that we do have the right Fermi surface.
- The choice of our interaction parameters is restricted in such a manner that, from the Wannier model defined above, we recover the correct peak positions of the interacting spin-spin susceptibility as measured in experiments.

The FS and the density of states (DOS) obtained from this downfolded t_{2g} model are displayed in Fig. 1. The left column corresponds to the unstrained system ($\epsilon_{xx} = 0$) and the right columns to the optimally uniaxially strained system for which the Fermi level is at the vHs ($\epsilon_{xx} = \epsilon_{xx}^{vHs}$). Note that ϵ_{xx}^{vHs} does not include quasi-particle renormalization and therefore is not the same value as in experiments. The D_{4h} space group symmetry of the unstrained system is lowered down to D_{2h} by uniaxial strain and the B_{1g} irreducible representation of D_{4h}, of greatest relevance to our study, turns into the A_g irreducible representation of D_{2h}.

Note the slightly unusual presentation of the FS in Fig. 1: this is due to the transformation from a tetragonal basis into a x–y plane which has to be done in this fashion to ensure the periodicity of the downfolded model in the two-dimensional primitive cell. Due to this, we have not a single but two k_z values in the first primitive cell, i.e., the Z-point is located at the corner of the black square. All the results that follow are obtained for the quasi-2D model restricted to $k_z = 0$ and $k_z = 2\pi/c$, shown in Fig. 1. We verify that they agree with the results from full 3D calculations in Supplementary Note 6.

The lowering of the symmetry under uniaxial strain lifts the degeneracy between the d_{xz} and the d_{yz} orbitals of the ruthenium atom, as seen in the DOS in Fig. 2. It also splits the d_{xy} van-Hove singularity into two parts: one drifting away from the FS (x-direction) and one drifting towards the FS and crosses it at the Lifschitz transition ($\epsilon_{xx}^{vHs} \sim 0.8\%$ strain). On the FS shown in Fig. 2, we also highlight the dominant nesting vectors of the bare particle-hole susceptibility (χ^0_{PH}), see Supplementary Note 2. First, $q_1 = (2\pi(3a)^{-1}, \pi(3b)^{-1})$ (and all those related by symmetry) connects the α and β sheets of the FS. Second, $q_2 = (\pi(2a)^{-1}, \pi(2b)^{-1})$ is connecting two van-Hove singularities and should become relevant at large interactions. Third, $q_3 = (\pi(3a)^{-1}, \pi(3a)^{-1})$ also connects the α and β sheet of the FS. These vectors are consistent with the dominant spin-fluctuations observed in neutron scattering experiments[90,116]. Note that there is a family of nesting vectors connecting α and β sheets, all close to q_1.

With these insights from the non-interacting FS and DOS in mind, we proceed with the phase diagrams as a function of U and J for the unstrained and the $\epsilon_{xx} = \epsilon_{xx}^{vHs}$ cases. The results are presented in Fig. 2. The background color corresponds to the energy scale Λ_c (expressed in meV) at which a divergence of the corresponding coupling is observed. The fastest divergent coupling corresponds to the dominant instability, which can either be superconductivity (in which case Λ_c is expected to be proportional to the Berezinskii-Kosterlitz-Thouless[117–119] critical temperature T_{BKT}) or a spin-density wave (SDW) (in which case Λ_c can be interpreted as the characteristic scale associated with the growth of the correlation length) (Because of Mermin-Wagner theorem (which is not obeyed by FRG), a finite T_c is expected for the BKT transition into the SC phase, while $T_c = 0$ for an SDW breaking $SU(2)$).

At the lowest U and J values, we find no divergence down to the lowest energy scale resolvable with our momentum resolution and thus conclude that the system remains in the Fermi-liquid (FL) state down to that scale. Apart from this unique point, we find three types of instabilities. Up to moderate U and low but finite J, we find a $d_{x^2-y^2}$ superconducting instability (corresponding to B_{1g} symmetry for the unstrained system, turning into A_g for the strained one). Upon increasing U or J, we find that the dominant instability becomes an SDW with ordering vector q_1. At even larger U and J, the system undergoes a high-temperature transition to another SDW phase characterized by the ordering vector q_2. These ordering vectors are visible in both non-interacting and interacting susceptibilities. Since we do not incorporate the effect of the self-energy, we cannot observe the shift of the q_3 peak observed in ref. 55.

Phase diagram and magnetic orderings

The q_1-SDW is driven by strong nesting between the α and β sheets. A corresponding peak in the spin-spin susceptibility has been well discussed both in the context of experimental observations[6,120] and theoretical discussions[54,67]. It should be noted that this vector connects two different values of k_z when backfolded in the three-dimensional Brillouin-zone. Its in-plane analog, $q_3 = (\pi(3a)^{-1}, \pi(3a)^{-1})$, was found to be subleading in earlier three-dimensional studies using the random phase approximation (RPA)[54]. The q_3 peak is also found in DMFT calculations including vertex corrections[55,121]. Here, we find the q_1 ordering to be the leading one, with the q_3 ordering also diverging but with a smaller absolute magnitude. The

increase of Λ_c can be understood in terms of the Stoner criterion being fulfilled at a larger scale for larger U or J. At higher energy scales, the vHs are strongly smeared. This effect increases the importance of the q_2 ordering vector connecting two vHs points, leading to the emergence of the q_2-SDW phase.

When applying uniaxial strain, the parameter range where we find an SDW is increased. This can be understood from the increase of the DOS at the Fermi level, which leads to a larger χ^0_{PH} and thereby a smaller interaction is required to fulfill the Stoner criterion. Beyond this effect, straining does not affect the structures of the phases and the q_2-phase is still observable in the same parameter region, as the changes of the FS due to strain have counteracting effects: while in the y-direction the FS touches the vHs, drifts further away from it in the x-direction.

Note that as we increase the strain beyond the Lifschitz transition, we do not find the SDW that is observed in experiments[38,41]. The emergence of this phase has been understood as the removal of all curvature of the γ sheet between the upper/lower vHs and the X/X' points, which leads to strong nesting along this direction[122]. We do not observe this phase at any investigated strain value. As was pointed out in ref. 123, strain suppresses quantum fluctuations preventing the ordered magnetic state, such that at high strain the phase transition emerges. Therefore, observing this transition in a diagrammatically unbiased approach is currently out of reach numerically, as it would require a full inclusion of the frequency dependence as well as multi-loop contributions[124]. We hope to overcome this shortcoming in the future.

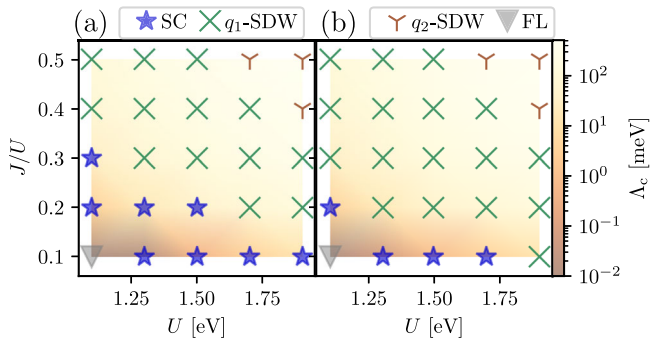

Fig. 2 | Phase diagrams in the *U*-*J* parameter space. In (**a**), we visualize the unstrained and in (**b**) the strained systems. The background color indicates the critical scale Λ_c, proportional to the ordering energy scale, with the corresponding colorbar on the right. The phases are either a B_{1g} superconductor (A_g under uniaxial strain), two different spin-density waves (SDWs), or a Fermi-liquid (FL). The q-vectors associated with the SDWs are shown in Fig. 1.

Superconductivity

In the following, the superconducting phase is analyzed using a linearized gap equation on the FS. As shown in Fig. 3, we find a gap that transforms according to a B_{1g} for $\epsilon_{xx} = 0$ (A_g for $\epsilon_{xx} = \epsilon^{\mathrm{vHs}}_{xx}$) representation of the D_{4h} (D_{2h}) point groups. In the band basis, this state has a dominant overlap with the $d_{x^2-y^2}$ harmonic and its main weight stems from the d_{xy} orbital. Such a type of superconductor has been observed in several other studies[53,54,58,59,66–68,122,125]. Although spin-orbit mixing distributes pairing over the different FS sheets, the dominant d_{xy} orbital character that we find does lead to a larger pairing on the γ sheet. It should be noted however that experiments indicate that the gap function is sizeable on all three Fermi surface sheets. This potential difficulty could be resolved by employing an analysis based on the combination of FRG and mean-field theory[126].

The spectrum of the pair-pair susceptibility at Λ_c contains the information of all possible subleading SCOPs. By analyzing this spectral distribution, we find a clear separation of the eigenvalue of the $d_{x^2-y^2}$ superconducting state by at least one order of magnitude from all eigenvalues of other SCOPs, for all parameters investigated. While this excludes any immediate degenerate state, no statement about the proximity of different symmetry states or individual critical temperatures can be drawn from FRG, because within this method the dominant instability is signaled by a divergent coupling and susceptibility (Again we stress that Λ_c is not to be confused with the leading eigenvalue from an Eliashberg calculation λ. Most importantly, we have $\Lambda_c \propto T_c$ instead of the exponential suppression from the gap equation). However, from the hierarchy standpoint, we still can extract tendencies toward different orderings as discussed in Supplementary Note 3. This hierarchy reveals that the p-wave pairing state[46,48,78] is always clearly subleading by a large margin and both extended s-wave and g-wave are consistently closer to the d-wave. We simulate the full 3D model at a selected point to check for the consistency of our 2D simulations. The results of these 3D simulations are shown in Supplementary Note 6 and agree with the 2D results.

The superconducting phase is generated by a spin-fluctuation mechanism. The couplings U and J are crucial tuning knobs determining the onset of the phase and also control the transition to the neighboring magnetic phase. When increasing U, the transition to an SDW is understood from the underlying ladder-type diagrams diverging as soon as U becomes larger than the critical value. Below that critical U, the still strong spin-fluctuations can drive a superconducting instability. However, increasing J has a more complex effect since it affects two different physical processes, which we discuss in terms of two distinct couplings, J_{ss} and J_{dd} in Eq. (1). J_{ss} promotes spin-flip and pair-hopping processes, thus reducing the tendency

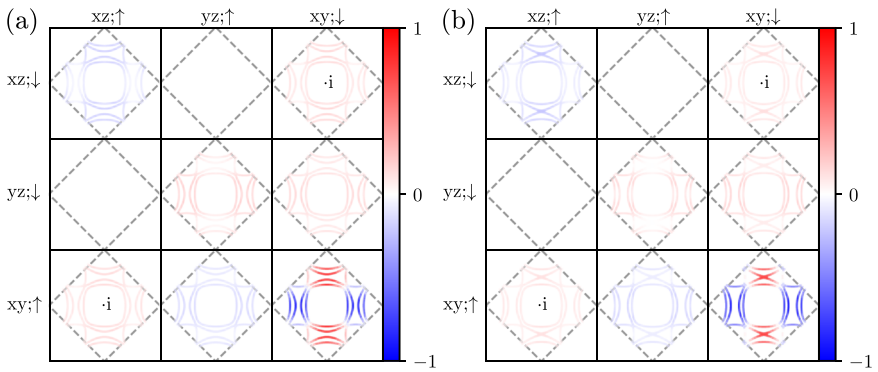

Fig. 3 | Example of superconducting order parameters found in Fig. 2, calculated from a linearized gap equation in orbital space. They correspond to $U = 1.1$ eV and $J = 0.22\,U$. The 3×3 matrices represent the spin-orbital states of the paired electrons in the inter-pseudospin channel since the intra-pseudospin terms are vanishing. Each panel shows the momentum structure. We present in **a**, **b** the unstrained case with $\epsilon_{xx} = 0$ and the optimally strained case with $\epsilon^{\mathrm{vHs}}_{xx}$ respectively. The SCOP transforms like the one-component B_{1g} (A_g) irreducible representation of the D_{4h} (D_{2h}) group which requires some components to be purely imaginary due to the transformation behavior of the spin-orbitals under rotational symmetries[68]. Since the gap function is only known up to a prefactor, we rescale it from −1 to 1, and the sign and value are encoded in the colorbar. The first Brillouin-zone is marked by the gray square.

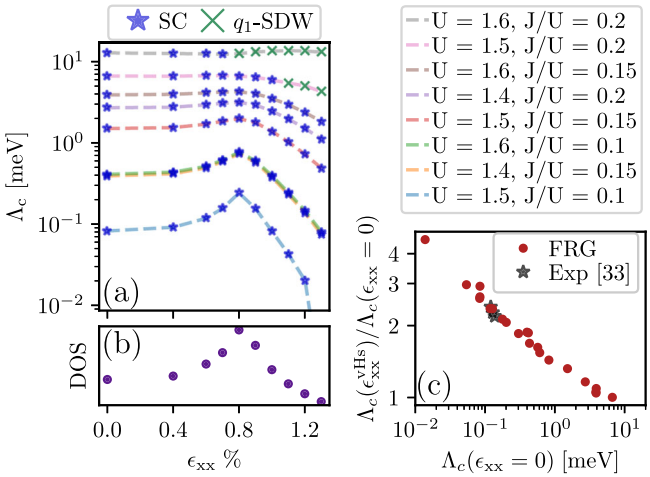

Fig. 4 | Effect of strain ϵ_{xx} on the critical scale Λ_c, the density of states and comparision to experiments. Effect of strain ϵ_{xx} on the critical scale Λ_c for different values of U and J (**a**) and values of U and J for each line given in the upper right. DOS in the d_{xy} orbital depends on ϵ (**b**) and theoretically predicted enhancement of Λ_c due to uniaxial strain as a function of its value for $\epsilon_{xx} = 0$ (**c**). Each dotted line in the upper left plot corresponds to one $U - J$ combination given in the upper right. There is a clear correlation between $\Lambda_c(\epsilon_{xx} = 0)$ and the ratio of increase in T_c which can be seen in both **a**, **c**. The experimental data points in **c** are extracted from ref. 33. A proposed mechanism that explains this enhancement is detailed in the text.

to order magnetically while also increasing pair-correlations. J_{dd} decreases inter-orbital density-density interactions, which reduces the inter-orbital repulsion between electrons on the same site. We unravel which of the two effects is most relevant for a) superconductivity and b) the magnetic transition. This is achieved by varying the two quantities independently, first in a simple RPA calculation and then in a full FRG calculation.

For the simple RPA calculation, we calculate χ^0_{PH} at $\Lambda = 11.6$ meV. We chose $U = 0.3$ eV to circumvent the Stoner instability and vary J_{ss} and J_{dd} between $0.0U$ and $0.3U$ independently. The dominant components of the bare susceptibility are presented in Supplementary Fig. 5 of Supplementary Note 4. In general, we observe that varying J_{ss} has barely any effect on χ^{RPA}_{PH}. J_{dd}, on the other hand, increases the inter-orbital components by a significant amount. Therefore we expect J_{ss} to have a weaker impact on the superconducting transition. Physically this is expected since J_{ss} hampers the spin-fluctuations that are required to obtain an effective attraction required by the superconducting state. To support this claim and understand better the underlying interference mechanism, we developed a simple 2-band toy model in Supplementary Note 4.

In the full FRG simulation, we verify these conclusions, i.e., increasing J_{ss} leads to a transition only at much larger values than the one for J_{dd}. See Supplementary Fig. 5. Interestingly, J_{ss} will generate a stronger admixture of higher-order angular momentum superconductivity hosted by the d_{yz} and d_{xz} orbitals. These are however still subleading to the $d_{x^2-y^2}$ superconducting state.

Influence of strain

Finally, we compare our results with experiments. We do so by examining the effect of strain from $\epsilon_{xx} = 0.0\%$ to $\epsilon_{xx} = 1.3\%$ on the leading instability of different (U, J) combinations. The general behavior of T_c is consistent with earlier studies[76,122,127], while the predicted phases partially differ. The different critical scales Λ_c can be interpreted as an estimate for T_c of the instability. The results for all superconducting data points are summarized in Fig. 4.

For systems that start with a large initial critical scale at zero strain ($\Lambda_c(\epsilon_{xx} = 0)$), no significant enhancement with respect to strain is found. The enhancement of T_c is much larger when $\Lambda(\epsilon_{xx} = 0)$ is smaller. This effect can be understood by looking at the DOS: large energy scales, or large temperatures, correspond to smeared-out features in the DOS. Thus, the shift of the vHs due to strain is irrelevant since the vHs are not resolved, i.e., the DOS at the Fermi level does not change under strain. The lower Λ_c, the sharper the vHs will become. Therefore, its shift enhances the DOS at the FS more strongly which in turn leads to a larger increase of T_c. Thus, a lower $\Lambda_c(\epsilon_{xx} = 0)$ yields an enhancement of T_c with ϵ_{xx} which is both larger and takes place over a narrower range of strain. Once the vHs have crossed the Fermi level, T_c is expected to go down again since we rapidly reduce the DOS at the Fermi level when straining further. Note that the nesting which generates the attractive interaction is not strongly asymmetric under strain, as can be seen in Fig. 1. Therefore, it cannot explain the asymmetry of Λ_C observed in Fig. 4. However, the density of states is asymmetric, see Fig. 4, giving rise to the observed asymmetry in Λ_C.

To compare our results to experiments, we evaluate $\Lambda_c(\epsilon_{xx}^{vHs})/\Lambda_c(\epsilon_{xx} = 0)$ and plot it versus $\Lambda_c(\epsilon_{xx} = 0)$, hence measuring the increase of the critical scale depending on the initial one. We extract the corresponding experimental values from ref. 33 by calculating the ratio of the maximal T_c and the T_c at $\epsilon_{xx} = 0$. These results are summarized in Fig. 4. We observe that the experiments indeed fit the data predicted by FRG and we can extract a line of U and J combinations along which the experiment is reproduced. We find that the values on the line are around $U = 1.1$, 1.4 eV, and $J = 0.143\ U$, $0.1\ U$. Again, we emphasize that these should be considered as effective values valid within our FRG formalism.

Discussion

In summary, we studied SRO starting from a first-principles description of its electronic structure and using a diagrammatically unbiased FRG approach. Using this framework, we investigated the influence of uniaxial strain as well as the different contributions of Hund's coupling. We identified that the inter-orbital interaction reduction due to the density-density term J_{dd} is the main driving force favoring superconducting order, which we found to be a pseudospin-singlet $d_{x^2-y^2}$. Lastly, we showed that the experimental increase of T_c as a function of strain can be recovered on a quantitative level from FRG simulations and from a comparison to these experiments we extracted effective values of the interaction parameters.

Our results highlight the dominance of a single $d_{x^2-y^2}$ SCOP that transforms like the B_{1g} representation (A_g under uniaxial strain). We note that, while this SCOP agrees with many experimental measurements, it cannot explain the evidence for two-components and time-reversal symmetry breaking. From the experimentally observed behavior of the time-reversal symmetry condition, we can infer that a partner of our found SCOP is required to remain invariant under moving the vHs through the Fermi level. This condition would be for example fulfilled by states with nodal lines along the x direction[60,61] or odd-frequency superconductors[68,69].

An interesting direction for future studies would be to investigate the effect of interaction terms consistent with D_{4h} symmetry but breaking full cubic symmetry. This could potentially influence the competition between different low-energy orders[109]. There are also many potential routes toward a more accurate investigation of the superconducting state. First, even though SRO is nearly perfectly layered, including the third spatial dimension increases the number of allowed ordering types[73]. Secondly, taking into account the frequency dependence of the gap function and self-energy would allow us to gauge the relevance of the proposed odd-frequency state. Finally, an important advance would be to start the FRG flow from a correlated starting point, i.e., from dressed quasi-particles and their effective interactions. This could for example be achieved by starting the FRG from a DMFT[128] description of the normal state.

Data availability

All simulation data is available upon reasonable request.

Code availability

The codes used for simulation are open-source packages and as such freely available.

Received: 19 July 2023; Accepted: 5 June 2024;
Published online: 09 July 2024

References

1. Maeno, Y. et al. Superconductivity in a layered perovskite without copper. *Nature* **372**, 532–534 (1994).
2. Rice, T. & Sigrist, M. Sr_2RuO_4: an electronic analogue of ^{3}He? *J. Condens. Matter Phys.* **7**, L643 (1995).
3. Ishida, K. et al. Spin-triplet superconductivity in Sr_2RuO_4 identified by ^{17}O knight shift. *Nature* **396**, 658–660 (1998).
4. Ishida, K. et al. Spin polarization enhanced by spin-triplet pairing in Sr_2RuO_4 probed by NMR. *Phys. Rev. B* **92**, 100502 (2015).
5. Duffy, J. A. et al. Polarized-neutron scattering study of the cooper-pair moment in Sr_2RuO_4. *Phys. Rev. Lett.* **85**, 5412–5415 (2000).
6. Braden, M. et al. Inelastic neutron scattering study of magnetic excitations in Sr_2RuO_4. *Phys. Rev. B* **66**, 064522 (2002).
7. Liu, Y., Nelson, K., Mao, Z., Jin, R. & Maeno, Y. Tunneling and phase-sensitive studies of the pairing symmetry in Sr_2RuO_4. *J. Low Temp. Phys.* **131**, 1059–1068 (2003).
8. Nelson, K., Mao, Z., Maeno, Y. & Liu, Y. Odd-parity superconductivity in Sr_2RuO_4. *Science* **306**, 1151–1154 (2004).
9. Liu, Y. Phase-sensitive-measurement determination of odd-parity, spin-triplet superconductivity in Sr_2RuO_4. *N. J. Phys.* **12**, 075001 (2010).
10. Deguchi, K., Mao, Z. Q., Yaguchi, H. & Maeno, Y. Gap structure of the spin-triplet superconductor Sr_2RuO_4 determined from the field-orientation dependence of the specific heat. *Phys. Rev. Lett.* **92**, 047002 (2004).
11. Lupien, C. et al. Ultrasound attenuation in Sr_2RuO_4: an angle-resolved study of the superconducting gap function. *Phys. Rev. Lett.* **86**, 5986–5989 (2001).
12. Xia, J., Maeno, Y., Beyersdorf, P. T., Fejer, M. M. & Kapitulnik, A. High resolution polar kerr effect measurements of Sr_2RuO_4: Evidence for broken time-reversal symmetry in the superconducting state. *Phys. Rev. Lett.* **97**, 167002 (2006).
13. Luke, G. M. et al. Time-reversal symmetry-breaking superconductivity in Sr_2RuO_4. *Nature* **394**, 558–561 (1998).
14. Mackenzie, A. P. & Maeno, Y. The superconductivity of Sr_2RuO_4 and the physics of spin-triplet pairing. *Rev. Mod. Phys.* **75**, 657–712 (2003).
15. Maeno, Y., Kittaka, S., Nomura, T., Yonezawa, S. & Ishida, K. Evaluation of spin-triplet superconductivity in Sr_2RuO_4. *J. Phys. Soc. Jpn.* **81**, 011009 (2012).
16. Izawa, K. et al. Superconducting gap structure of spin-triplet superconductor Sr_2RuO_4 studied by thermal conductivity. *Phys. Rev. Lett.* **86**, 2653–2656 (2001).
17. Hassinger, E. et al. Vertical line nodes in the superconducting gap structure of Sr_2RuO_4. *Phys. Rev. X* **7**, 011032 (2017).
18. Tanatar, M. A. et al. Anisotropy of magnetothermal conductivity in Sr_2RuO_4. *Phys. Rev. Lett.* **86**, 2649–2652 (2001).
19. Nishizaki, S., Maeno, Y. & Mao, Z. Changes in the superconducting state of Sr_2RuO_4 under magnetic fields probed by specific heat. *J. Phys. Soc. Jpn.* **69**, 572–578 (2000).
20. Jerzembeck, F. et al. Upper critical field of Sr_2RuO_4 under in-plane uniaxial pressure. *Phys. Rev. B* **107**, 064509 (2023).
21. Kittaka, S. et al. Sharp magnetization jump at the first-order superconducting transition in Sr_2RuO_4. *Phys. Rev. B* **90**, 220502 (2014).
22. Yonezawa, S., Kajikawa, T. & Maeno, Y. Specific-heat evidence of the first-order superconducting transition in Sr_2RuO_4. *J. Phys. Soc. Jpn.* **83**, 083706 (2014).
23. Kinjo, K. et al. Superconducting spin smecticity evidencing the Fulde-Ferrell-Larkin-Ovchinnikov state in Sr_2RuO_4. *Science* **376**, 397–400 (2022).
24. Kirtley, J. R. et al. Upper limit on spontaneous supercurrents in Sr_2RuO_4. *Phys. Rev. B* **76**, 014526 (2007).
25. Hicks, C. W. et al. Limits on superconductivity related magnetization in Sr_2RuO_4 and $PrOs_4Sb_{12}$ from scanning squid microscopy. *Phys. Rev. B* **81**, 214501 (2010).
26. Curran, P. J. et al. Search for spontaneous edge currents and vortex imaging in Sr_2RuO_4 mesostructures. *Phys. Rev. B* **89**, 144504 (2014).
27. Kreisel, A. et al. Quasi-particle interference of the van Hove singularity in Sr_2RuO_4. *npj Quant. Mater.* **6**, 100 (2021).
28. Scaffidi, T. & Simon, S. H. Large chern number and edge currents in Sr_2RuO_4. *Phys. Rev. Lett.* **115**, 087003 (2015).
29. Pustogow, A. et al. Constraints on the superconducting order parameter in Sr_2RuO_4 from oxygen-17 nuclear magnetic resonance. *Nature* **574**, 72–75 (2019).
30. Ishida, K., Manago, M., Kinjo, K. & Maeno, Y. Reduction of the ^{17}O knight shift in the superconducting state and the heat-up effect by NMR pulses on Sr_2RuO_4. *J. Phys. Soc. Jpn.* **89**, 034712 (2020).
31. Petsch, A. N. et al. Reduction of the spin susceptibility in the superconducting state of Sr_2RuO_4 observed by polarized neutron scattering. *Phys. Rev. Lett.* **125**, 217004 (2020).
32. Watson, C. A., Gibbs, A. S., Mackenzie, A. P., Hicks, C. W. & Moler, K. A. Micron-scale measurements of low anisotropic strain response of local T_c in Sr_2RuO_4. *Phys. Rev. B* **98**, 094521 (2018).
33. Steppke, A. et al. Strong peak in T_c of Sr_2RuO_4 under uniaxial pressure. *Science* **355**, eaaf9398 (2017).
34. Chronister, A. et al. Tuning the Fermi liquid crossover in Sr_2RuO_4 with uniaxial stress. *npj Quant. Mater.* **7**, 113 (2022).
35. Sunko, V. et al. Direct observation of a uniaxial stress-driven Lifshitz transition in Sr_2RuO_4. *npj Quant. Mater.* **4**, 46 (2019).
36. Benhabib, S. et al. Ultrasound evidence for a two-component superconducting order parameter in Sr_2RuO_4. *Nat. Phys.* **17**, 194–198 (2021).
37. Ghosh, S. et al. Thermodynamic evidence for a two-component superconducting order parameter in Sr_2RuO_4. *Nat. Phys.* **17**, 199–204 (2021).
38. Grinenko, V. et al. Split superconducting and time-reversal symmetry-breaking transitions in Sr_2RuO_4 under stress. *Nat. Phys.* **17**, 748–754 (2021).
39. Grinenko, V. et al. μSR measurements on Sr_2RuO_4 under $\langle 110 \rangle$ uniaxial stress. *Phys. Rev. B* **107**, 024508 (2023).
40. Li, Y.-S. et al. High-sensitivity heat-capacity measurements on Sr_2RuO_4 under uniaxial pressure. *Proc. Natl Acad. Sci. USA* **118**, e2020492118 (2021).
41. Li, Y.-S. et al. Elastocaloric determination of the phase diagram of Sr_2RuO_4. *Nature* **607**, 276–280 (2022).
42. Palle, G. et al. Constraints on the superconducting state of Sr_2RuO_4 from elastocaloric measurements. *Phys. Rev. B* **108**, 094516 (2023).
43. Mueller, E. et al. Constraints on a split superconducting transition under uniaxial strain in Sr_2RuO_4 from scanning SQUID microscopy. *Phys. Rev. B* **108**, 144501 (2023).
44. Mackenzie, A. P., Scaffidi, T., Hicks, C. W. & Maeno, Y. Even odder after twenty-three years: the superconducting order parameter puzzle of Sr_2RuO_4. *npj Quant. Mater.* **2**, 40 (2017).
45. Raghu, S., Kapitulnik, A. & Kivelson, S. A. Hidden quasi-one-dimensional superconductivity in Sr_2RuO_4. *Phys. Rev. Lett.* **105**, 136401 (2010).
46. Wang, Q. et al. Theory of superconductivity in a three-orbital model of Sr_2RuO_4. *Europhys. Lett.* **104**, 17013 (2013).
47. Tsuchiizu, M., Yamakawa, Y., Onari, S., Ohno, Y. & Kontani, H. Spin-triplet superconductivity in Sr_2RuO_4 due to orbital and spin fluctuations: analyses by two-dimensional renormalization group theory and self-consistent vertex-correction method. *Phys. Rev. B* **91**, 155103 (2015).
48. Wang, W.-S., Zhang, C.-C., Zhang, F.-C. & Wang, Q.-H. Theory of chiral p-wave superconductivity with near nodes for Sr_2RuO_4. *Phys. Rev. Lett.* **122**, 027002 (2019).

49. Zhang, L.-D., Huang, W., Yang, F. & Yao, H. Superconducting pairing in Sr_2RuO_4 from weak to intermediate coupling. *Phys. Rev. B* **97**, 060510 (2018).
50. Scaffidi, T., Romers, J. C. & Simon, S. H. Pairing symmetry and dominant band in Sr_2RuO_4. *Phys. Rev. B* **89**, 220510 (2014).
51. Ramires, A. & Sigrist, M. Identifying detrimental effects for multiorbital superconductivity: Application to Sr_2RuO_4. *Phys. Rev. B* **94**, 104501 (2016).
52. Acharya, S. et al. Evening out the spin and charge parity to increase t_c in Sr_2RuO_4. *Commun. Phys.* **2**, 163 (2019).
53. Rømer, A. T., Hirschfeld, P. J. & Andersen, B. M. Superconducting state of Sr_2RuO_4 in the presence of longer-range Coulomb interactions. *Phys. Rev. B* **104**, 064507 (2021).
54. Rømer, A. T., Maier, T. A., Kreisel, A., Hirschfeld, P. J. & Andersen, B. M. Leading superconducting instabilities in three-dimensional models for Sr_2RuO_4. *Phys. Rev. Res.* **4**, 033011 (2022).
55. Moon, C.-Y. Effects of orbital selective dynamical correlation on the spin susceptibility and superconducting symmetries in Sr_2RuO_4. *Phys. Rev. Res.* **5**, L022058 (2023).
56. Røising, H. S., Wagner, G., Roig, M., Rømer, A. T. & Andersen, B. M. Heat capacity double transitions in time-reversal symmetry broken superconductors. *Phys. Rev. B* **106**, 174518 (2022).
57. Kivelson, S. A., Yuan, A. C., Ramshaw, B. & Thomale, R. A proposal for reconciling diverse experiments on the superconducting state in Sr_2RuO_4. *npj Quant. Mater.* **5**, 43 (2020).
58. Sheng, Y., Li, Y. & Yang, Y.-f Multipole-fluctuation pairing mechanism of $d_{x^2-y^2} + ig$ superconductivity in Sr_2RuO_4. *Phys. Rev. B* **106**, 054516 (2022).
59. Wang, X., Wang, Z. & Kallin, C. Higher angular momentum pairing states in Sr_2RuO_4 in the presence of longer-range interactions. *Phys. Rev. B* **106**, 134512 (2022).
60. Yuan, A. C., Berg, E. & Kivelson, S. A. Strain-induced time reversal breaking and half quantum vortices near a putative superconducting tetracritical point in Sr_2RuO_4. *Phys. Rev. B* **104**, 054518 (2021).
61. Yuan, A. C., Berg, E. & Kivelson, S. A. Multiband mean-field theory of the d + ig superconductivity scenario in Sr_2RuO_4. *Phys. Rev. B* **108**, 014502 (2023).
62. Scaffidi, T. Degeneracy between even- and odd-parity superconductivity in the quasi-one-dimensional Hubbard model and implications for Sr_2RuO_4. *Phys. Rev. B* **107**, 014505 (2023).
63. Kaba, S.-O. & Sénéchal, D. Group-theoretical classification of superconducting states of strontium ruthenate. *Phys. Rev. B* **100**, 214507 (2019).
64. Ando, S., Ikegaya, S., Tamura, S., Tanaka, Y. & Yada, K. Surface state of the interorbital pairing state in the Sr_2RuO_4 superconductor. *Phys. Rev. B* **106**, 214520 (2022).
65. Nica, E. M. & Si, Q. Multiorbital singlet pairing and d+d superconductivity. *npj Quant. Mater.* **6**, 3 (2021).
66. Deisz, J. J. & Kidd, T. E. Quantum many-body calculation of mixed-parity pairing in the Sr_2RuO_4 superconductor induced by spin-orbit coupling. *Phys. Rev. Lett.* **107**, 277003 (2011).
67. Gingras, O., Nourafkan, R., Tremblay, A.-M. S. & Côté, M. Superconducting symmetries of Sr_2RuO_4 from first-principles electronic structure. *Phys. Rev. Lett.* **123**, 217005 (2019).
68. Gingras, O., Allaglo, N., Nourafkan, R., Côté, M. & Tremblay, A.-M. S. Superconductivity in correlated multiorbital systems with spin-orbit coupling: Coexistence of even- and odd-frequency pairing, and the case of Sr_2RuO_4. *Phys. Rev. B* **106**, 064513 (2022).
69. Gingras, O., Georges, A. & Parcollet, O. Frequency-dependent superconducting states from the two-time linear response theory: application to Sr_2RuO_4. *arXiv*:2312.15074 (2023).
70. Suh, H. G. et al. Stabilizing even-parity chiral superconductivity in Sr_2RuO_4. *Phys. Rev. Res.* **2**, 032023 (2020).
71. Beck, S., Hampel, A., Zingl, M., Timm, C. & Ramires, A. Effects of strain in multiorbital superconductors: The case of Sr_2RuO_4. *Phys. Rev. Res.* **4**, 023060 (2022).
72. Huang, W. & Yao, H. Possible three-dimensional nematic odd-parity superconductivity in Sr_2RuO_4. *Phys. Rev. Lett.* **121**, 157002 (2018).
73. Ramires, A. & Sigrist, M. Superconducting order parameter of Sr_2RuO_4: a microscopic perspective. *Phys. Rev. B* **100**, 104501 (2019).
74. Metzner, W., Salmhofer, M., Honerkamp, C., Meden, V. & Schönhammer, K. Functional renormalization group approach to correlated fermion systems. *Rev. Mod. Phys.* **84**, 299–352 (2012).
75. Kohn, W. & Sham, L. J. Self-consistent equations including exchange and correlation effects. *Phys. Rev.* **140**, A1133–A1138 (1965).
76. Liu, Y.-C., Zhang, F.-C., Rice, T. M. & Wang, Q.-H. Theory of the evolution of superconductivity in Sr_2RuO_4 under anisotropic strain. *npj Quant. Mater.* **2**, 12 (2017).
77. Wang, Z., Wang, X. & Kallin, C. Spin-orbit coupling and spin-triplet pairing symmetry in Sr_2RuO_4. *Phys. Rev. B* **101**, 064507 (2020).
78. Liu, Y.-C., Wang, W.-S., Zhang, F.-C. & Wang, Q.-H. Superconductivity in Sr_2RuO_4 thin films under biaxial strain. *Phys. Rev. B* **97**, 224522 (2018).
79. Hohenberg, P. & Kohn, W. Inhomogeneous electron gas. *Phys. Rev.* **136**, B864–B871 (1964).
80. Kohn, W., Becke, A. D. & Parr, R. G. Density functional theory of electronic structure. *J. Phys. Chem.* **100**, 12974–12980 (1996).
81. Giannozzi, P. et al. Quantum espresso: a modular and open-source software project for quantum simulations of materials. *J. Condens. Matter Phys.* **21**, 395502 (2009).
82. Giannozzi, P. et al. Advanced capabilities for materials modelling with quantum ESPRESSO. *J. Condens. Matter Phys.* **29**, 465901 (2017).
83. Perdew, J. P., Burke, K. & Ernzerhof, M. Generalized gradient approximation made simple. *Phys. Rev. Lett.* **77**, 3865–3868 (1996).
84. Garrity, K. F., Bennett, J. W., Rabe, K. M. & Vanderbilt, D. Pseudopotentials for high-throughput dft calculations. *Comput. Mater. Sci.* **81**, 446–452 (2014).
85. Takeda, T. The scalar relativistic approximation. *Zeitschrift für Physik B Condens. Matter* **32**, 43–48 (1978).
86. Mostofi, A. A. et al. wannier90: a tool for obtaining maximally-localised wannier functions. *Comput. Phys. Commun.* **178**, 685–699 (2008).
87. Mostofi, A. A. et al. An updated version of wannier90: A tool for obtaining maximally-localised wannier functions. *Comput. Phys. Commun.* **185**, 2309–2310 (2014).
88. Pizzi, G. et al. Wannier90 as a community code: new features and applications. *J. Condens. Matter Phys.* **32**, 165902 (2020).
89. Kanamori, J. Electron correlation and ferromagnetism of transition metals. *Prog. Theor. Phys.* **30**, 275–289 (1963).
90. Steffens, P. et al. Spin fluctuations in Sr_2RuO_4 from polarized neutron scattering: Implications for superconductivity. *Phys. Rev. Lett.* **122**, 047004 (2019).
91. Dupuis, N. et al. The nonperturbative functional renormalization group and its applications. *Phys. Rep.* **910**, 1–114 (2021).
92. Scherer, M. M., Kennes, D. M. & Classen, L. Chiral superconductivity with enhanced quantized hall responses in moiré transition metal dichalcogenides. *npj Quant. Mater.* **7**, 100 (2022).
93. Klebl, L., Fischer, A., Classen, L., Scherer, M. M. & Kennes, D. M. Competition of density waves and superconductivity in twisted tungsten diselenide. *Phys. Rev. Res.* **5**, L012034 (2023).
94. Gneist, N., Classen, L. & Scherer, M. M. Competing instabilities of the extended Hubbard model on the triangular lattice: truncated-unity functional renormalization group and application to moiré materials. *Phys. Rev. B* **106**, 125141 (2022).

95. Kiesel, M. L., Platt, C., Hanke, W. & Thomale, R. Model evidence of an anisotropic chiral $d+id$-wave pairing state for the water-intercalated $Na_xCoO_2 \cdot yH_2O$ superconductor. *Phys. Rev. Lett.* **111**, 097001 (2013).
96. Kiesel, M. L., Platt, C. & Thomale, R. Unconventional fermi surface instabilities in the kagome hubbard model. *Phys. Rev. Lett.* **110**, 126405 (2013).
97. Beyer, J. et al. Rashba spin-orbit coupling in the square-lattice Hubbard model: A truncated-unity functional renormalization group study. *Phys. Rev. B* **107**, 125115 (2023).
98. Kiesel, M. L., Platt, C., Hanke, W., Abanin, D. A. & Thomale, R. Competing many-body instabilities and unconventional superconductivity in graphene. *Phys. Rev. B* **86**, 020507 (2012).
99. Profe, J. B., Honerkamp, C., Achilles, S. & Kennes, D. M. Electronic instabilities in Penrose quasicrystals: Competition, coexistence, and collaboration of order. *Phys. Rev. Res.* **3**, 023180 (2021).
100. Ehrlich, J. & Honerkamp, C. Functional renormalization group for fermion lattice models in three dimensions: Application to the hubbard model on the cubic lattice. *Phys. Rev. B* **102**, 195108 (2020).
101. Klebl, L., Kennes, D. M. & Honerkamp, C. Functional renormalization group for a large moiré unit cell. *Phys. Rev. B* **102**, 085109 (2020).
102. de la Peña, D. S., Lichtenstein, J., Honerkamp, C. & Scherer, M. M. Antiferromagnetism and competing charge instabilities of electrons in strained graphene from coulomb interactions. *Phys. Rev. B* **96**, 205155 (2017).
103. O, S.-J., Kim, Y.-H., Rim, H.-Y., Pak, H.-C. & Im, S.-J. Effect of exchange interaction on electronic instabilities in the honeycomb lattice: a functional renormalization group study. *Phys. Rev. B* **99**, 245140 (2019).
104. Beyer, J., Profe, J. B. & Klebl, L. Reference results for the momentum space functional renormalization group. *Eur. Phys. J. B* **95**, 65 (2022).
105. Husemann, C. & Salmhofer, M. Efficient parametrization of the vertex function, Ω scheme, and the t, t' Hubbard model at van Hove filling. *Phys. Rev. B* **79**, 195125 (2009).
106. Lichtenstein, J. et al. High-performance functional renormalization group calculations for interacting fermions. *Comput. Phys. Commun.* **213**, 100 – 110 (2017).
107. Profe, J. B. & Kennes, D. M. TU_2FRG: a scalable approach for truncated unity functional renormalization group in generic fermionic models. *Eur. Phys. J. B* **95**, 60 (2022).
108. Tamai, A. et al. High-resolution photoemission on Sr_2RuO_4 reveals correlation-enhanced effective spin-orbit coupling and dominantly local self-energies. *Phys. Rev. X* **9**, 021048 (2019).
109. Zhang, G., Gorelov, E., Sarvestani, E. & Pavarini, E. Fermi surface of Sr_2RuO_4: Spin-orbit and anisotropic Coulomb interaction effects. *Phys. Rev. Lett.* **116**, 106402 (2016).
110. Kim, M., Mravlje, J., Ferrero, M., Parcollet, O. & Georges, A. Spin-orbit coupling and electronic correlations in Sr_2RuO_4. *Phys. Rev. Lett.* **120**, 126401 (2018).
111. Veenstra, C. N. et al. Spin-orbital entanglement and the breakdown of singlets and triplets in Sr_2RuO_4 revealed by spin- and angle-resolved photoemission spectroscopy. *Phys. Rev. Lett.* **112**, 127002 (2014).
112. Haverkort, M. W., Elfimov, I. S., Tjeng, L. H., Sawatzky, G. A. & Damascelli, A. Strong spin-orbit coupling effects on the fermi surface of Sr_2RuO_4 and Sr_2RhO_4. *Phys. Rev. Lett.* **101**, 026406 (2008).
113. Pavarini, E. & Mazin, I. I. First-principles study of spin-orbit effects and NMR in Sr_2RuO_4. *Phys. Rev. B* **74**, 035115 (2006).
114. Damascelli, A. et al. Fermi surface, surface states, and surface reconstruction in Sr_2RuO_4. *Phys. Rev. Lett.* **85**, 5194–5197 (2000).
115. Barber, M. E. et al. Role of correlations in determining the van Hove strain in Sr_2RuO_4. *Phys. Rev. B* **100**, 245139 (2019).
116. Iida, K. et al. Inelastic neutron scattering study of the magnetic fluctuations in Sr_2RuO_4. *Phys. Rev. B* **84**, 060402 (2011).
117. Berezinskii, V. Destruction of long-range order in one-dimensional and two-dimensional systems having a continuous symmetry group i. classical systems. *Sov. Phys. JETP* **32**, 493–500 (1971).
118. Berezinskii, V. Destruction of long-range order in one-dimensional and two-dimensional systems possessing a continuous symmetry group. ii. quantum systems. *Sov. Phys. JETP* **34**, 610–616 (1972).
119. Kosterlitz, J. M. & Thouless, D. J. Ordering, metastability and phase transitions in two-dimensional systems. *J. Phys. C Solid State Phys.* **6**, 1181 (1973).
120. Iida, K. et al. Two-dimensional incommensurate magnetic fluctuations in $Sr_2(Ru_{0.99}Ti_{0.01})O_4$. *J. Phys. Soc. Jpn.* **81**, 124710 (2012).
121. Strand, H. U. R., Zingl, M., Wentzell, N., Parcollet, O. & Georges, A. Magnetic response of Sr_2RuO_4: Quasi-local spin fluctuations due to Hund's coupling. *Phys. Rev. B* **100**, 125120 (2019).
122. Rømer, A. T. et al. Theory of strain-induced magnetic order and splitting of T_c and T_{trsb} in Sr_2RuO_4. *Phys. Rev. B* **102**, 054506 (2020).
123. Kim, B., Khmelevskyi, S., Franchini, C. & Mazin, I. I. Suppressed fluctuations as the origin of the static magnetic order in strained Sr_2RuO_4. *Phys. Rev. Lett.* **130**, 026702 (2023).
124. Hille, C. et al. Quantitative functional renormalization group description of the two-dimensional Hubbard model. *Phys. Rev. Res.* **2**, 033372 (2020).
125. Roig, M., Rømer, A. T., Kreisel, A., Hirschfeld, P. J. & Andersen, B. M. Superconductivity in multiorbital systems with repulsive interactions: Hund's pairing versus spin-fluctuation pairing. *Phys. Rev. B* **106**, L100501 (2022).
126. Wang, J., Eberlein, A. & Metzner, W. Competing order in correlated electron systems made simple: consistent fusion of functional renormalization and mean-field theory. *Phys. Rev. B* **89**, 121116 (2014).
127. Lindquist, A. W. & Kee, H.-Y. Distinct reduction of knight shift in superconducting state of Sr_2RuO_4 under uniaxial strain. *Phys. Rev. Res.* **2**, 032055 (2020).
128. Taranto, C. et al. From infinite to two dimensions through the functional renormalization group. *Phys. Rev. Lett.* **112**, 196402 (2014).
129. Thörnig, P. Jülich Supercomputing Centre. JURECA: Data Centric and Booster Modules implementing the Modular Supercomputing Architecture at Jülich Supercomputing Centre. *J. Large-Scale Res. Facilit.* **7**, A182 (2021).

Acknowledgements

JBP thanks Prof. E. Pavarini, Friedrich Krien, Lennart Klebl, and Jacob Beyer for the helpful discussion. The authors gratefully acknowledge the computing time granted through JARA on the supercomputer JURECA[129] at Forschungszentrum Jülich. JBP and DMK are supported by the Deutsche Forschungsgemeinschaft (DFG, German Research Foundation) under RTG 1995, within the Priority Program SPP 2244 "2DMP"—443273985 and under Germany's Excellence Strategy—Cluster of Excellence Matter and Light for Quantum Computing (ML4Q) EXC 2004/1—390534769. The Flatiron Institute is a division of the Simons Foundation.

Author contributions

S.B. performed the DFT simulations. J.B.P. performed the FRG simulations. J.B.P., A.G., and O.G. analyzed the results. J.B.P., A.B., D.M.K., A.G., and OG contributed to writing the Manuscript.

Funding

Open Access funding enabled and organized by Projekt DEAL.

Competing interests

The authors declare no competing interests.

Additional information

Supplementary information The online version contains supplementary material available at https://doi.org/10.1038/s41535-024-00661-3.

Correspondence and requests for materials should be addressed to Jonas B. Profe.